

An Axial Velocity Estimator for Ultrasound Blood Flow Imaging, Based on a Full Evaluation of the Doppler Equation by Means of a Two-Dimensional Autocorrelation Approach

Thanasis Loupas, J. T. Powers, *Member, IEEE*, and Robert W. Gill, *Member, IEEE*

Abstract— This paper introduces a new velocity estimator, referred to as the 2D autocorrelator, which differs from conventional Doppler techniques in two respects: the derivation of axial velocity values by evaluating the Doppler equation using explicit estimates of both the mean Doppler and the mean RF frequency at each range gate location; and, the 2D nature (depth samples versus pulse transmissions) of processing within the range gate. The estimator's output can be calculated by evaluating the 2D autocorrelation function of the demodulated (baseband) backscattered echoes at two lags. A full derivation and mathematical description of the estimator is presented, based on the framework of the 2D Fourier transform. The same framework is adopted to analyze two other established velocity estimators (the conventional 1D autocorrelator and the crosscorrelator) in a unifying manner, and theoretical arguments as well as experimental results are used to highlight the common aspects of all three estimators. In addition, a thorough performance evaluation is carried out by means of extensive simulations, which document the effect of a number of factors (velocity spread, range gate length, ensemble length, noise level, transmitted bandwidth) and provide an insight into the optimum parameters and trade-offs associated with individual algorithms. Overall, the 2D autocorrelator is shown to offer the best performance in the context of the specific simulation conditions considered here. Its superiority over the crosscorrelator is restricted to cases of low signal-to-noise ratios. However, the 2D autocorrelator always outperforms the conventional 1D autocorrelator by a significant margin. These comparisons, when linked to the computational requirements of the proposed estimator, suggest that it combines the generally higher performance of 2D broadband time-domain techniques with the relatively modest complexity of 1D narrowband phase-domain velocity estimators.

I. INTRODUCTION

EXISTING COLOR flow mapping techniques for axial velocity estimation can be classified according to a number of schemes. Common classification criteria and corresponding terminologies include the type of input data (demodulated/RF) and its dimensionality (one-dimensional/two-

dimensional or 1D/2D),¹ the domain on which the estimators operate (frequency/phase/time) and the typical transmitted bandwidths associated with them (narrowband/broadband). Despite this diversity, it is important to recognize that all techniques take advantage of the same physical principle: the gradual translation of the backscattered signal, with respect to previous pulse returns, due to the changing distance between the transducer and groups of moving scatterers. In the case of blood, the backscattered signal is mainly due to aggregates of erythrocytes. Although these aggregates are of a generally time-varying nature, nevertheless, they exhibit a degree of temporal stability which permits the ultrasonic measurement of blood flow [1].

The gradual translation of the backscattered signal is manifested both as a phase- and a time-shift between successive pulse returns. With very few exceptions, commercial color flow scanners use a phase-domain technique, known as the autocorrelator [2], [3], for axial velocity estimation. This algorithm measures the average phase-shift, with respect to the central frequency of the transmitted pulse, present in the complex-valued Doppler signal (the signal recorded at a given range gate, over a number of pulses, after it has undergone phase quadrature demodulation). This is a 1D approach, because the echoes received from each range gate are reduced to one (complex) value per pulse through filtering or integration of the demodulated in-phase and quadrature (I & Q) signal. Also, it could be classified as a narrowband approach, in the sense that typical pulse lengths are considerably longer than the corresponding pulse lengths used in B-mode imaging [4].

In contrast to 1D narrowband phase-shift techniques such as the autocorrelator, a number of broadband processing schemes have been proposed recently, which estimate the axial velocity of moving targets directly in the time domain by operating on the 2D set of received echoes (depth samples versus pulse transmissions). These include: crosscorrelation techniques, which measure the time-shift corresponding to the best match between successive RF returns [5]–[10]; maximum-

Manuscript received May 23, 1994; revised December 5, 1994.

T. Loupas and R. W. Gill are with the Ultrasonics Laboratory, Division of Radiophysics-CSIRO, Chatswood NSW 2067, Australia.

J. E. Powers is with the Advanced Technology Laboratories, Bothell WA 98041 USA.

IEEE Log Number 9411954.

¹Throughout this paper, the notation "2D" refers to the dimensionality (depth samples versus pulse transmissions) of the input data set used for axial velocity estimation. Therefore, it should not be confused with two-dimensional (axial and lateral component) velocity techniques, or processing schemes related to two-dimensional transducer arrays.

likelihood estimators, based on a matched filter approach which explicitly takes into account all the velocity components present in the backscattered signal [11], [12]; interpolation methods, which rely on a model of the expected RF correlation between successive returns and a few measured lags to estimate the mean time-shift [13]–[15]. A comprehensive survey of time-domain techniques can be found in [16].

This paper examines a novel estimator which combines the generally higher performance of 2D broadband time-domain techniques with the relatively modest complexity of 1D narrowband phase-domain estimators, in terms of both the number of computations per output point and the sampling rate requirements. The estimator, which could be classified as a 2D broadband phase-domain technique, relies on a two-dimensional autocorrelation approach to obtain estimates of both the mean Doppler and RF frequencies of the signal inside the observation window. These estimates permit a full evaluation of the Doppler equation and, consequently, address the unrealistic assumption, made by all phase-domain techniques so far, that the RF frequency of the backscattered signal remains constant and equal to the central frequency of the transmitted pulse.

The paper is organized in the following manner. Section II derives the mathematical form of the new estimator, based on first principles, and introduces a modification which permits processing of baseband signals. The conventional 1D autocorrelator [2], [3] and the crosscorrelator [5]–[10] are also analyzed in this section, with emphasis on theoretical results from the signal processing literature and a unifying description which highlights the common aspects of the estimators. Section III describes the simulation approach which was adopted to compare the performance of the three estimators in a systematic manner. The results of the comparisons, which encompass factors such as the velocity spread, range gate and ensemble length, noise level and transmitted bandwidth, are presented in Section IV. Finally, the concluding remarks of this study are summarized in Section V.

II. AXIAL VELOCITY ESTIMATORS

The following terminology is used throughout this and subsequent sections: the terms “range gate length” and “ensemble length” specify the number of depth samples and number of pulse transmissions, respectively, which are used to derive an axial velocity estimate; the terms “fast-time” and “slow-time” refer to the axes along the range gate and ensemble directions; the frequencies corresponding to the fast- and slow-time axes (RF and Doppler, respectively) are denoted by f_{RF} and F_D when they are expressed in absolute units, or by f and F when they are normalized in terms of the fast- or slow-time sampling rates (i.e., $f = f_{\text{RF}}t_s$ and $F = F_D T_s$, where t_s is the sampling interval along depth and T_s is the pulse repetition period); finally, when referring to 2D arrays (say, $r(m, n)$), the first index (m) specifies the column number whereas the second index (n) specifies the row number.

A. Two-Dimensional Autocorrelator

The starting point for the derivation of the 2D autocorrelator is the two-dimensional Fourier transform of successive RF

returns, which have been acquired by interrogating a fixed line of sight with a sequence of pulses and arranged as a 2D data set, with the number of rows and columns corresponding to the transmitted pulses and range gate samples, respectively. This approach, whose relevance for pulsed Doppler has been independently demonstrated in [17] and [18], provides a comprehensive and unifying framework for analyzing the problem of axial velocity estimation, because it deals explicitly with the gradual translation principle mentioned in the Introduction. Wilson [18] has shown that when successive RF returns are translated versions of each other, due to target motion, the 2D spectrum is nonzero only along radial line segments of the frequency plane whose slope is proportional to the amount of translation.

The following two paragraphs make use of the results in [19], which studied analytically the problem of 2D spectral analysis for discrete limited-duration signals. The case of a line of scatterers moving towards the transducer with a purely axial velocity v is considered first. The transducer is assumed to transmit T_s pulses per second, of the type

$$s(t) = \text{Re}[u(t)e^{j2\pi f_{\text{RF}}t}] \quad (1)$$

where $u(t)$ and f_{RF} are the pulse's envelope and central frequency, respectively. Then, from [19], the analog backscattered RF signal due to the n -th transmission can be written as

$$\begin{aligned} r^a(t, n) &= s(t) * \left[\sum_i a_i \delta \left(t - t_{i0} + \frac{2nvT_s}{c} \right) \right] \\ &= r^a \left(t + \frac{2nvT_s}{c}, 0 \right) \end{aligned} \quad (2)$$

where $*$ is the convolution operator, δ the unit-impulse function, a_i the scattering strength of target i , and t_{i0} the echo reception from the same target during the 0-th emission. The above equation states that for the case of purely axial motion, the rows of the 2D data set $r^a(t, n)$ are shifted versions of each other. Again from [19], the 2D spectrum of a discrete version of $r^a(t, n)$, consisting of N pulse returns of M depth samples each, is

$$\begin{aligned} \Gamma(f, F) &= \left| \left(R_0(f) \delta \left(F - f \frac{2vT_s}{ct_s} \right) \right) \right. \\ &\quad * \left(\frac{\sin[\pi f M]}{M \sin[\pi f]} e^{-j\pi f(M-1)} \right) \\ &\quad \left. * \left(\frac{\sin[\pi F N]}{N \sin[\pi F]} e^{-j\pi F(N-1)} \right) \right|^2 \end{aligned} \quad (3)$$

where t_s is the sampling interval along depth, f and F the normalized RF and Doppler frequencies and $R_0(f)$ the discrete Fourier transform of a sampled version of the 0th return $r^a(t, 0)$. Assuming for the moment that M and N are sufficiently large such that the spectral windows in (3) become impulses, the above equation states that $\Gamma(f, F)$ is zero everywhere, apart from the line passing through the origin of the frequency plane and having a slope F/f equal to $2vT_s/ct_s$. On that line, $\Gamma(f, F)$ consists of exponential random variables multiplied by the bandpass spectrum $|S(f)|^2$

of the transmitted pulse $s(t)$, resulting in two line segments centered around plus and minus the normalized central RF frequency f_c [19]. In other words, for a given normalized RF frequency f' within the pulse bandwidth, the 2D spectrum is nonzero only for a normalized Doppler frequency F' equal to $2vT_s f' / ct_s$. Using absolute frequency notation ($F'_D = F' / T_s$, $f'_{RF} = f' / t_s$) this becomes $F'_D = 2v f'_{RF} / c$. Thus, the familiar Doppler equation applies for all RF frequencies within the transmitted bandwidth. Returning now to the realistic case of finite M and N , convolution with the separable spectral windows in (3) causes smearing of the 2D spectrum, so that the ideal line segments become elliptical masses. This is a manifestation of spectra broadening due to the limited extent of the observation window [18]. In addition to broadening, the process of spectral convolution introduces a degree of correlation between neighboring points of the 2D frequency plane, which can become quite significant for a short range gate and/or ensemble length.

By means of the superposition principle, the above analysis can be extended to the case of scatterers arranged in concentric annulae which share the same axis as the beam and move towards the transducer with different velocities. For this arrangement, the analog backscattered RF signal is

$$r^a(t, n) = s(t) * \left[\sum_k D(r_k) \sum_i a_{ki} \delta \left(t - t_{ki0} + \frac{2nv_k T_s}{c} \right) \right] \quad (4)$$

where the subscript k specifies a particular annulus of scatterers having the same axial velocity v_k , $D(r_k)$, refers to the lateral sensitivity of the transducer with respect to an annulus at a radius r_k from the beam axis, and the remaining symbols are defined as in (2). The corresponding power spectrum of a sampled and finite-extent version of $r^a(t, n)$ is then equal to

$$\Gamma(f, F) = \left| \left(\sum_k R_{0k}(f) D(r_k) \delta \left(F - f \frac{2v_k T_s}{ct_s} \right) \right) * \left(\frac{\sin[\pi f M]}{M \sin[\pi f]} e^{-j\pi f(M-1)} \right) * \left(\frac{\sin[\pi F N]}{N \sin[\pi F]} e^{-j\pi F(N-1)} \right) \right|^2 \quad (5)$$

where $R_{0k}(f)$ denotes the Fourier transform of the convolution between the pulse $s(t)$ and the 0th return due to the k th annulus of scatterers. In this case, the 2D spectrum consists of exponential random variables distributed along as many radial line segments as the number of velocity components present in the backscattered RF signal.

The previous two paragraphs and, in particular, the points referring to the stochastic nature of the 2D spectrum, imply that while the mean RF frequency $\langle f \rangle$ may fluctuate randomly, the corresponding mean Doppler frequency $\langle F \rangle$ tracks these fluctuations so that their ratio $\langle F \rangle / \langle f \rangle$ is constant and proportional to the mean axial velocity. An experimental illustration of this phenomenon is presented in Fig. 1, which is discussed later in this section. The fact that the mean RF and Doppler frequencies vary considerably, even for constant flow, but they also tend to track each other has been previously documented

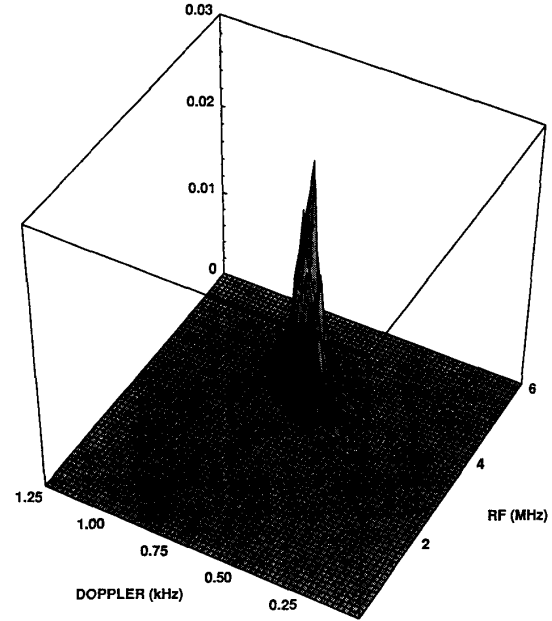


Fig. 1. Histogram of the estimated mean Doppler and RF frequencies, obtained by applying the 2D autocorrelator to data from a tissue-mimicking belt phantom, moving at a constant velocity (see text for acquisition and processing details).

in [20], where it was mentioned as a serious drawback of the conventional 1D autocorrelator which assumes that the mean RF frequency is constant and equal to the central frequency of the transmitted pulse. This drawback can be overcome by deriving estimates of both the mean Doppler and mean RF frequency for each location of the observation window. The most straightforward approach would be to estimate the mean axial velocity from the slope of the line passing through the origin of the frequency plane and through the center of mass of the 2D spectrum in either the positive ($0 \leq f < 0.5$) or negative ($-0.5 \leq f < 0$) frequency semiplane. The 2D autocorrelation estimator implements this approach directly in the time domain.

Due to the properties of the 2D Fourier transform for real signals [21, ch. 1.3]), the spectrum $\Gamma(f, F)$ is symmetric with respect to the origin of the frequency plane. Therefore, in order to identify its center of mass in either the positive or negative semiplane, the symmetry must be removed. This can be achieved by means of the analytic signal version of the backscattered RF echoes. For the discrete case, the analytic signal $\hat{r}(m, n)$ of $r(m, n)$ is defined as

$$\hat{r}(m, n) = r(m, n) - j\check{r}(m, n) \quad (6)$$

where $\check{r}(m, n)$ denotes the discrete 1D Hilbert transform of $r(m, n)$ along depth

$$\check{r}(m, n) = \frac{-1}{\pi n} * r(m, n) \quad (7)$$

A direct consequence of the Hilbert transform's properties [22, ch. 12] is that the Fourier transform $\hat{R}(f, F)$ of the

analytic signal $\hat{r}(m, n)$ is zero for the semiplane defined by $-0.5 \leq f < 0$

$$\hat{R}(f, F) = \begin{cases} 2R(f, F) & 0 \leq f < 0.5 \\ 0 & -0.5 \leq f < 0 \end{cases} \quad (8)$$

and, assuming that clutter has already been removed, the center of mass of the 2D spectrum in the positive semiplane coincides with the centroid of the entire 2D spectrum $\hat{\Gamma}(f, F) = |\hat{R}(f, F)|^2$. The center of mass is located at point $\{\langle f \rangle, \langle F \rangle\}$, whose coordinates are the mean normalized frequencies along the RF and Doppler frequency axis, respectively.

$$\langle f \rangle = \frac{\int_{-0.5}^{0.5} \int_{-0.5}^{0.5} f \hat{\Gamma}(f, F) df dF}{\int_{-0.5}^{0.5} \int_{-0.5}^{0.5} \hat{\Gamma}(f, F) df dF} \quad (9)$$

$$\langle F \rangle = \frac{\int_{-0.5}^{0.5} \int_{-0.5}^{0.5} F \hat{\Gamma}(f, F) df dF}{\int_{-0.5}^{0.5} \int_{-0.5}^{0.5} \hat{\Gamma}(f, F) df dF} \quad (10)$$

Appendix A shows that $\langle f \rangle$ and $\langle F \rangle$ can be estimated directly in the time domain by evaluating the phase of the autocorrelation function $\hat{\gamma}(m', n')$ of the analytic signal $\hat{r}(m, n)$

$$\hat{\gamma}(m', n') = \sum_{m=0}^{M-m'-1} \sum_{n=0}^{N-n'-1} \hat{r}(m, n) \hat{r}^*(m+m', n+n') \quad (11)$$

at lags $(m' = 1, n' = 0)$ and $(m' = 0, n' = 1)$, where it has been assumed that the observation window consists of M depth samples $(m = 0, 1, \dots, M-1)$ and N pulse returns $(n = 0, 1, \dots, N-1)$. More specifically

$$\langle f \rangle = \frac{-j \frac{\partial \hat{\gamma}(m', n')}{\partial m'} \Big|_{m'=n'=0}}{\hat{\gamma}(0, 0)} \cong \frac{1}{2\pi} \tan^{-1} \left\{ \frac{\text{Im}[\hat{\gamma}(1, 0)]}{\text{Re}[\hat{\gamma}(1, 0)]} \right\} \quad (12)$$

$$\langle F \rangle = \frac{-j \frac{\partial \hat{\gamma}(m', n')}{\partial n'} \Big|_{m'=n'=0}}{\hat{\gamma}(0, 0)} \cong \frac{1}{2\pi} \tan^{-1} \left\{ \frac{\text{Im}[\hat{\gamma}(0, 1)]}{\text{Re}[\hat{\gamma}(0, 1)]} \right\} \quad (13)$$

Since the slope of the line passing through the origin of the frequency plane and the centroid $\{\langle f \rangle, \langle F \rangle\}$ is equal to $2\langle v \rangle T_s / ct_s$, the mean velocity estimate $\langle v_{2D} \rangle$ provided by the 2D autocorrelator can then be evaluated from

$$\langle v_{2D} \rangle = \frac{ct_s \langle F \rangle}{2T_s \langle f \rangle} \cong \frac{ct_s}{2T_s} \frac{\tan^{-1} \left\{ \frac{\text{Im}[\hat{\gamma}(0, 1)]}{\text{Re}[\hat{\gamma}(0, 1)]} \right\}}{\tan^{-1} \left\{ \frac{\text{Im}[\hat{\gamma}(1, 0)]}{\text{Re}[\hat{\gamma}(1, 0)]} \right\}} \quad (14)$$

which can be rearranged, using absolute frequency notation

$$\langle v_{2D} \rangle = \frac{c}{2} \frac{\frac{1}{2\pi T_s} \tan^{-1} \left\{ \frac{\text{Im}[\hat{\gamma}(0, 1)]}{\text{Re}[\hat{\gamma}(0, 1)]} \right\}}{\frac{1}{2\pi T_s} \tan^{-1} \left\{ \frac{\text{Im}[\hat{\gamma}(1, 0)]}{\text{Re}[\hat{\gamma}(1, 0)]} \right\}} = \frac{c}{2} \frac{\langle F_D \rangle}{\langle f_{RF} \rangle} \quad (15)$$

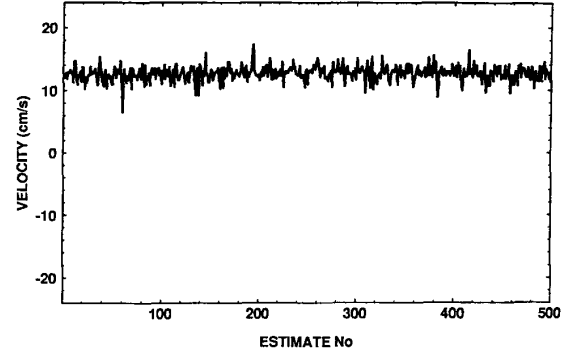


Fig. 2. Sequence of axial velocity estimates provided by the 2D autocorrelator, using a subset of the input data set of Fig. 1.

to highlight the fact that the 2D autocorrelator performs a full evaluation of the Doppler equation.

The benefits of this approach can be appreciated from Fig. 1, which plots the histogram of estimated Doppler and RF mean frequencies for an ensemble length equal to two pulses ($N = 2$), a range gate length equal to twenty samples ($M = 20$) and 16,000 observation windows. The input data for this figure were obtained by interrogating a tissue-mimicking belt phantom [23] moving at a constant velocity of 24.5 cm s^{-1} . The angle of insonation was approximately 60° , the 20-dB pulse length corresponded to four wavelengths of the central RF frequency, which was equal to 4 MHz, the sampling RF rate was 20 MHz ($t_s = 50 \text{ ns}$) and the pulse repetition frequency was 2.5 kHz ($T_s = 0.4 \text{ ms}$). From this figure, it is obvious that both the Doppler and RF mean frequency estimates fluctuate considerably about their true values but, at the same time, they tend to be distributed along radial line segments of the 2D frequency plane. By averaging the individual Doppler and RF estimates, it was verified that the slope of the line passing through the origin of the frequency plane and the centroid of the estimates is equal to the predicted value of $\langle F_D \rangle / \langle f_{RF} \rangle = 2v \cos \theta / c = 1.59 \times 10^{-4}$. A sequence of axial velocity estimates, derived from a subset of the input data mentioned above, is plotted in Fig. 2, while the velocity estimates obtained from the same data using the conventional 1D autocorrelator and crosscorrelator are shown in Figs. 4 and 7, respectively.

A desirable property of the 2D autocorrelator is that, apart from the analytic RF signal, it can also be applied to the complex demodulated (in-phase and quadrature, or I & Q) signal. More specifically, it can be shown [24, ch. 6.1] that quadrature demodulation of an RF signal using $f_{RF \text{ dem}}$ as the reference frequency is equivalent to shifting the contents of the analytic RF signal's spectrum by $f_{RF \text{ dem}}$ towards zero. If

$$z(m, n) = I(m, n) + jQ(m, n) \quad (16)$$

represents the demodulated version of the RF signal $r(m, n)$, the above statement implies that the spectrum of $z(m, n)$ is given by

$$|Z(f, F)|^2 = |\hat{R}(f + f_{\text{dem}}, F)|^2 = \hat{\Gamma}(f + f_{\text{dem}}, F) \quad (17)$$

where the symbol f_{dem} denotes the normalized counterpart of the absolute frequency $f_{\text{RF dem}}$ of the reference sinusoid. Therefore, when the 2D autocorrelator estimator is applied to the complex demodulated signal $z(m, n)$, the measured mean Doppler frequency remains unchanged, while the factor f_{dem} must be added to the measured mean RF frequency to take into account the shift towards zero. The following equation, modified from (15), describes the mean velocity obtained from the 2D autocorrelator for the case of the complex demodulated signal $z(m, n)$:

$$\langle v_{2D} \rangle = \frac{c}{2} \frac{\frac{1}{2\pi T_s} \tan^{-1} \left\{ \frac{\text{Im}[\gamma_{\text{dem}}(0, 1)]}{\text{Re}[\gamma_{\text{dem}}(0, 1)]} \right\}}{\frac{1}{2\pi T_s} \left(2\pi f_{\text{dem}} + \tan^{-1} \left\{ \frac{\text{Im}[\gamma_{\text{dem}}(1, 0)]}{\text{Re}[\gamma_{\text{dem}}(1, 0)]} \right\} \right)} \quad (18)$$

where γ_{dem} is the 2D autocorrelation function of $z(m, n)$

$$\begin{aligned} \gamma_{\text{dem}}(m', n') &= \sum_{m=0}^{M-m'-1} \sum_{n=0}^{N-n'-1} z(m, n) z^*(m+m', n+n') \\ &= \sum_{m=0}^{M-m'-1} \sum_{n=0}^{N-n'-1} [I(m, n)I(m+m', n+n') \\ &\quad + Q(m, n)Q(m+m', n+n')] \\ &\quad + j \sum_{m=0}^{M-m'-1} \sum_{n=0}^{N-n'-1} [Q(m, n)I(m+m', n+n') \\ &\quad - I(m, n)Q(m+m', n+n')] \end{aligned} \quad (19)$$

Finally, (18) and (19) can be combined to express the mean velocity in terms of the I & Q samples according to (20). Equation (15)—the analytic RF version—and (18) or (20)—the I & Q version—are mathematically equivalent. However, the latter is highly advantageous from an implementation point of view, because the I & Q signal is already available in most scanners. In addition, baseband processing requires a significantly lower sampling rate compared to RF processing, which is translated directly into hardware simplicity and computational efficiency.

As discussed further in Subsection II-B, the 2D autocorrelator differs from the conventional 1D autocorrelator in terms of two factors: (a) the explicit estimation of the mean RF frequency; (b) the 2D algorithmic form used in deriving

mean Doppler frequency estimates. Both factors contribute to performance gains, as documented in the results of Section IV which compares the output statistics of the 2D autocorrelator, conventional 1D autocorrelator and crosscorrelator for a wide range of operating parameters and signal characteristics.

B. One-Dimensional Autocorrelator

The 1D autocorrelator [2] represented the breakthrough that enabled color flow mapping to be implemented in real-time. The same algorithm is used even today by the majority of commercial scanners. The estimator is one-dimensional, in the sense that it is applied to the complex demodulated (I & Q) signal after its values along the depth axis are collapsed into a single point per pulse. This can be achieved either by filtering the I & Q signal obtained from a pulse emission and retaining only one value per sample volume, or by integrating the I & Q signal along the extent of the range gate. This reduction in the dimensionality of the data is identical to that used in conventional PW Doppler where, in the filtering case, the filter's frequency response is matched to the spectrum of the pulse's envelope and, in the integration case, the range gate is chosen to be equal to the pulse length, due to noise considerations [25]. While filtering and integration appear to be very similar in the context of PW Doppler [25], the latter option has been chosen here because of its mathematical tractability, while filtering is examined only implicitly. Before proceeding with the 1D autocorrelator, the spectral content of the integrated Doppler signal must be specified. Starting from the complex demodulated signal $z(m, n)$ of (16), its integrated version can be expressed as

$$\begin{aligned} z_{\text{int}}(n) &= \sum_{m=0}^{M-1} z(m, n) = I_{\text{int}}(n) + jQ_{\text{int}}(n) \\ &= \sum_{m=0}^{M-1} I(m, n) + j \sum_{m=0}^{M-1} Q(m, n) \end{aligned} \quad (21)$$

The 1D integrated Doppler signal $z_{\text{int}}(n)$ can be thought of as providing the average phase of the signal inside the sample volume, with respect to the frequency of the reference sinusoid used in the demodulation process. The spectral content of $z_{\text{int}}(n)$ can be related to the 2D Fourier transform framework by observing that the integration described by (21) is equivalent to a projection of the 2D array $z(m, n)$

$$\langle v_{2D} \rangle \cong \frac{c}{2} \frac{\frac{1}{2\pi T_s} \tan^{-1} \left\{ \frac{\sum_{m=0}^{M-1} \sum_{n=0}^{N-2} [Q(m, n)I(m, n+1) - I(m, n)Q(m, n+1)]}{\sum_{m=0}^{M-1} \sum_{n=0}^{N-2} [I(m, n)I(m, n+1) + Q(m, n)Q(m, n+1)]} \right\}}{\frac{1}{2\pi T_s} \left(2\pi f_{\text{dem}} + \tan^{-1} \left\{ \frac{\sum_{m=0}^{M-2N-1} \sum_{n=0}^{M-2N-1} [Q(m, n)I(m+1, n) - I(m, n)Q(m+1, n)]}{\sum_{m=0}^{M-2N-1} \sum_{n=0}^{M-2N-1} [I(m, n)I(m+1, n) + Q(m, n)Q(m+1, n)]} \right\} \right)} \quad (20)$$

along the horizontal (depth) axis. Due to the projection-slice theorem [26], the 1D Fourier transform $Z_{\text{int}}(F)$ of $z_{\text{int}}(n)$ is the vertical slice of the 2D Fourier transform $Z(f, F)$ of $z(m, n)$ at $f = 0$. By making use of (17), the 1D spectrum $|Z_{\text{int}}(F)|^2$ can now be written as

$$|Z_{\text{int}}(F)|^2 = |Z(0, F)|^2 = \hat{\Gamma}(f_{\text{dem}}, F) \quad (22)$$

In other words, the spectrum of the integrated I & Q Doppler signal coincides with the column of the 2D analytic RF spectrum that passes through f_{dem} . While this result is mathematically correct and has also been verified in terms of numerical examples, the following clarification must be made, to avoid potential misunderstandings. The measured 2D analytic RF spectrum $\hat{\Gamma}(f, F)$, obtained by means of 2D Fourier analysis, is only a distorted version of the ideal 2D spectrum (see the discussion following expression (3), in Subsection II-A). In particular, convolution of the ideal 2D Fourier transforms with the separable spectral windows in (3) or (5) means that each column of the measured 2D analytic RF spectrum includes contributions from adjacent columns.

An alternative approach for deriving (22) is to treat integration as a combination of two operations: (a) filtering the rows of $z(m, n)$ by convolving their real and imaginary parts with a window function $w(i) = 1, i = 0, \dots, M-1$, and (b) obtaining a single filtered I & Q sample per pulse return, by retaining only the output I & Q sample which is located at the center of the window. Since convolution of two functions in the time domain corresponds to their product in the frequency domain [24, ch. 4.3], operation (a) is equivalent to row-wise multiplication of the 2D Fourier transform $Z(f, F)$ of $z(m, n)$ by the Fourier transform $W(f)$ of the window function $w(i)$ where, for the case of integration, $W(f)$ is in fact equal to the unit-impulse function $\delta(f)$. Based on the properties of this function [24, ch. 2.3], the product $Z(f, F)\delta(f)$ is given by $Z(0, F)$ for $f = 0$, and zero everywhere else. Now, due to the inverse form of the projection-slice theorem [26], operation (b)—a vertical slice through the 2D array of filtered I & Q samples in the time domain—corresponds to a projection of the 2D Fourier transform $Z(f, F)\delta(f)$ onto the Doppler (F) axis, which is simply equal to $Z(0, F)$. Hence, the spectrum of the integrated I & Q Doppler signal is given by (22). While this proof may not be as elegant as that of the previous paragraph, it does emphasize the similarities that exist between filtering and integration, and provides a straightforward methodology for determining the spectral content of the filtered Doppler signal for arbitrary filter coefficients.

Returning now to the 1D autocorrelator, its function is to extract the mean frequency of the integrated Doppler signal by means of time-domain operations. By taking into account (22) and invoking the 2D frequency plane arguments originally mentioned in Subsection II-A, the 1D autocorrelator can be considered as estimating the mean velocity from the slope of the line passing through the origin of the frequency plane and the centroid of the analytic RF spectrum's column at $f = f_{\text{dem}}$, where f_{dem} denotes the normalized frequency of the reference sinusoid used in the demodulation. In other words, a mean velocity estimate is derived from the 1D integrated Doppler signal according to

$$\langle v_{1D} \rangle = \frac{ct_s \langle F \rangle|_{f=f_{\text{dem}}}}{2T_s f_{\text{dem}}} \quad (23)$$

with

$$\langle F \rangle|_{f=f_{\text{dem}}} = \frac{\int_{-0.5}^{0.5} F \hat{\Gamma}(f_{\text{dem}}, F) dF}{\int_{-0.5}^{0.5} \hat{\Gamma}(f_{\text{dem}}, F) dF} \quad (24)$$

The spectral centroid $\langle F \rangle|_{f=f_{\text{dem}}}$ can be calculated directly in the signal domain by making use of a theorem which states that the spectral moments of a signal can be evaluated in terms of the derivatives of its autocorrelation function [22, ch. 8]. Since the derivation is well known (e.g., see [2] or [3, ch. 6.6.2]) and a two-dimensional version of it has been included in Appendix A, it will not be repeated here. It suffices to state that if the autocorrelation of the 1D integrated Doppler signal is given by

$$\gamma_{\text{int}}(n') = \sum_{n=0}^{N-n'-1} z_{\text{int}}(n) z_{\text{int}}^*(n+n') \quad (25)$$

then, the mean Doppler frequency $\langle F \rangle|_{f=f_{\text{dem}}}$ is

$$\langle F \rangle|_{f=f_{\text{dem}}} \cong \frac{1}{2\pi} \tan^{-1} \left\{ \frac{\text{Im}[\gamma_{\text{int}}(1)]}{\text{Re}[\gamma_{\text{int}}(1)]} \right\} \quad (26)$$

which can be incorporated into (23) to give

$$\langle v_{1D} \rangle = \frac{c}{2} \frac{\frac{1}{2\pi T_s} \tan^{-1} \left\{ \frac{\text{Im}[\gamma_{\text{int}}(1)]}{\text{Re}[\gamma_{\text{int}}(1)]} \right\}}{\frac{f_{\text{dem}}}{t_s}} \quad (27)$$

By making use of (25), (21), and (16), (28) is obtained.

Equation (28) has been expressed explicitly in terms of the I & Q samples, so that direct comparisons can be made with

$$\langle v_{1D} \rangle = \frac{c}{2} \frac{\frac{1}{2\pi T_s} \tan^{-1} \left\{ \frac{\sum_{n=0}^{N-2} \left[\sum_{m=0}^{M-1} Q(m, n) \sum_{m=0}^{M-1} I(m, n+1) - \sum_{m=0}^{M-1} I(m, n) \sum_{m=0}^{M-1} Q(m, n+1) \right]}{\sum_{n=0}^{N-2} \left[\sum_{m=0}^{M-1} I(m, n) \sum_{m=0}^{M-1} I(m, n+1) + \sum_{m=0}^{M-1} Q(m, n) \sum_{m=0}^{M-1} Q(m, n+1) \right]} \right\}}{\frac{f_{\text{dem}}}{t_s}} \quad (28)$$

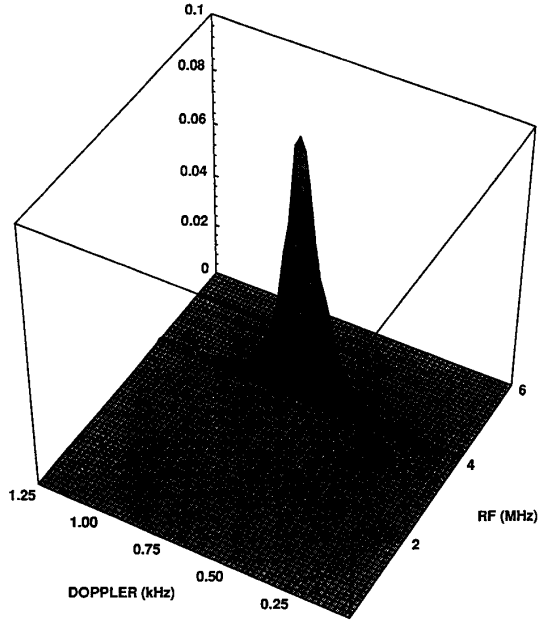


Fig. 3. Histogram of the estimated mean Doppler frequencies, obtained by applying the 1D autocorrelator to the input data set of Fig. 1. Note that the 3D histogram format of Fig. 1 has also been adopted here to facilitate comparisons.

the corresponding form of the 2D autocorrelator in (20). The following two differences are observed. First, as far as the RF frequency value required for the evaluation of the Doppler equation is concerned, the 1D autocorrelator assumes that it is constant and equal to the frequency of the reference sinusoid used in the demodulation (which is typically the central frequency of the RF pulse), instead of estimating it at each depth location of the observation window. Second, with regards to the mean Doppler frequency, the 1D autocorrelator collapses the I & Q data into one complex value per pulse return before performing correlation along the slow-time axis, unlike the 2D autocorrelator which incorporates explicitly the contributions of all I & Q samples into the frequency estimation process. The effect of these differences is illustrated in Figs. 3 and 4, which have been based on the same data (as well as range gate and ensemble length) and are therefore directly comparable to Figs. 1 and 2, respectively. Fig. 3 presents the histogram of the mean Doppler frequency estimates provided by the 1D autocorrelator, which exhibits noticeably heavier tails than the corresponding histogram tails of the 2D autocorrelator (Fig. 1). Further improvement is observed in the axial velocity estimates of the 2D autocorrelator of Fig. 2, compared with the output of the 1D autocorrelator in Fig. 4, because of the compensation for the RF frequency fluctuations.

An insight into the statistical properties of the 1D autocorrelator can be obtained from the theoretical results in [27]. Adapting the symbols used originally in [27] to maintain consistency with the notation of this paper, a complex Gaussian process (the true signal) is combined with another process of the same type (noise), to produce the observed signal. The

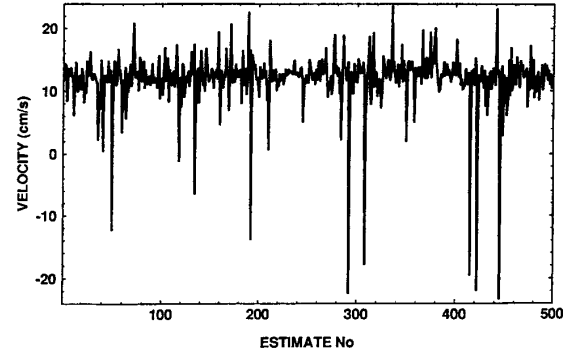


Fig. 4. Sequence of axial velocity estimates provided by the 1D autocorrelator. The input data set for this figure was the same as that used in Figs. 2 and 7.

autocorrelation of the combined process is then

$$\begin{aligned}\gamma(T') &= |\gamma(T')|e^{j2\pi\theta(T')} = \gamma_1(T') + \gamma_2(T') \\ &= |\gamma_1(T')|e^{j2\pi\theta_1(T')} + |\gamma_2(T')|e^{j2\pi\theta_2(T')}\end{aligned}\quad (29)$$

where subscripts 1 and 2 denote the true signal and noise, respectively. The standard deviation of the mean frequency estimate, as given in [27] is

$$\sigma = \left\{ \frac{|\gamma(0)|^2 - |\gamma(T')|^2 \cos 4\pi[\theta(T') - \theta_1(T')]}{8N\pi^2 T'^2 |\gamma_1(T')|^2} \right\}^{1/2} \quad (30)$$

where N denotes the number of samples and T' represents the lag value used in approximating the derivative of the autocorrelation function as a finite difference. This expression can be simplified in the case of white noise (i.e., $\gamma_2(T') = 0$ for $T' \neq 0$) and the dependence on the signal-to-noise ratio ($\text{SNR} = |\gamma_1(0)|/|\gamma_2(0)|$) can be made explicit.

$$\sigma = \left\{ \frac{\left(1 + \frac{1}{\text{SNR}}\right)^2 - \frac{|\gamma_1(T')|^2}{|\gamma_1(0)|^2}}{8N\pi^2 T'^2 \frac{|\gamma_1(T')|^2}{|\gamma_1(0)|^2}} \right\}^{1/2} \quad (32)$$

As a case study, let us assume that the spectrum of the true signal is Gaussian in shape with mean frequency F_μ and frequency spread F_σ . Then its autocorrelation is

$$\gamma_1(T') = \gamma_1(0)e^{-(2\pi F_\sigma T')^2/2}e^{-j2\pi F_\mu T'} \quad (33)$$

and rearrangement of (32) results in

$$\frac{N^{1/2}\sigma}{F_\sigma} = \left\{ \frac{\left(1 + \frac{1}{\text{SNR}}\right)^2 - e^{-x^2}}{2x^2 e^{-x^2}} \right\}^{1/2} \quad (34)$$

where the left-hand side of the equation represents the standard deviation of the 1D autocorrelator normalized in terms of the number of samples and the frequency spread, and the auxiliary variable x is defined as $x = 2\pi F_\sigma T'$. The standard deviation is plotted in Fig. 5 as a function of x , for SNRs varying from

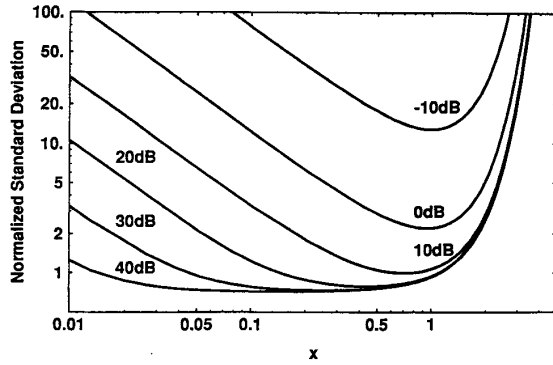


Fig. 5. Theoretically predicted standard deviation curves (from expression 34) of the 1D autocorrelator for six SNRs. The standard deviation has been normalized by multiplying it with a factor $N^{1/2}/F_\sigma$ and is plotted against the auxiliary variable $x = 2\pi F_\sigma T'$, where N is the number of pulses, F_σ the spectrum's frequency spread and T' the lag value used for evaluating the phase of the autocorrelation.

–10 to 40 dB in steps of 10 dB. Expression (34) implies that the standard deviation of the 1D autocorrelator:

- is independent of the mean frequency F_μ
- is inversely proportional to the square root of the number of samples N
- depends on a function of $1 + 1/\text{SNR}$
- has a complex relationship to the frequency spread F_σ which, as Fig. 5 illustrates, depends on both the lag value T' and the SNR.

The above statements may be correct for the signal of (33), but should be treated only as an approximation of the properties of the 1D autocorrelator in the context of color flow mapping. This is because the analysis in [27] is concerned with strictly 1D signals and, therefore, does not take into account phenomena related to the transformation of a 2D RF array into a 1D integrated I & Q sequence, nor does it address explicitly the issue of aliasing. An additional insight into the statistical properties of the 1D autocorrelator can be obtained from the theoretical analysis in [28].

In concluding this subsection, a number of techniques, which are also applied to the 1D integrated I & Q signal, should be mentioned. These include averaging of the instantaneous Doppler frequency [29] as well as variants of the 1D autocorrelator that use more than one correlation lag [30], [31] and estimators based on autoregressive models [32], [33]. In general, though, the performance of these techniques has not been shown to be consistently better than the 1D autocorrelator. This suggests that, at least for the case considered here, the specific form of an algorithm is less important than the information content of the input signal on which it operates.

C. Crosscorrelator

Unlike the 1D techniques mentioned in the previous subsection, the crosscorrelation estimator is applied directly to the received RF echoes and, therefore, has access to the full information carried by them. Crosscorrelation represents one of the fundamental and most thoroughly investigated tools in digital signal processing, and has been used extensively in a

number of applications involving time-delay estimation. Two comprehensive sources of information on the subject are the book by Bendat and Piersol [34] and a special issue of IEEE Transactions on Acoustics, Speech and Signal Processing [35].

The relevance of crosscorrelation for color flow mapping was first demonstrated by Bonnefous and Pesque [5], [6]. This work, in conjunction with the work by O'Brien's group [7]–[10], had a major impact, in the sense that it caused researchers in the field to reconsider the traditional Doppler frequency-shift paradigm and think of the mean velocity estimation issue in terms of the gradual shifts that the backscattered RF echoes experience between successive pulses. In its simplest form, the crosscorrelator estimates this shift by locating the maximum of the crosscorrelation function between two successive RF returns. For continuous and infinite-extent signals and just one velocity component, it is easy to show that this “best-match” approach provides the true shift. By making use of (2), the RF returns due to pulses n and $n + 1$ are

$$r^a(t, n) = r^a\left(t + \frac{2nvT_s}{c}, 0\right) \quad (35)$$

and

$$\begin{aligned} r^a(t, n+1) &= r^a\left(t + \frac{2(n+1)vT_s}{c}, 0\right) \\ &= r^a\left(t + \frac{2vT_s}{c}, n\right) \end{aligned} \quad (36)$$

respectively. The crosscorrelation between $r^a(t, n)$ and $r^a(t, n+1)$ is given by

$$\gamma_{\text{CRS}}(t') = \int_{-\infty}^{+\infty} r^a(t, n) r^a(t + t', n+1) dt \quad (37)$$

while the autocorrelation of $r^a(t, n)$, which is equal to the autocorrelation of $r^a(t, n+1)$, is

$$\begin{aligned} \gamma(t') &= \int_{-\infty}^{+\infty} r^a(t, n) r^a(t + t', n) dt \\ &= \int_{-\infty}^{+\infty} r^a(t, n+1) r^a(t + t', n+1) dt \end{aligned} \quad (38)$$

With the help of (36), it is straightforward to show that

$$\gamma_{\text{CRS}}(t') = \gamma\left(t' + \frac{2vT_s}{c}\right) \quad (39)$$

and since, with the exception of purely periodic functions, the autocorrelation $\gamma(t')$ of a signal has a global maximum at $t' = 0$

$$\gamma_{\text{CRS}}(t') \rightarrow \max \quad \text{for } t' = t'_0 = -\frac{2vT_s}{c} \quad (40)$$

Instead of searching for the peak of the crosscorrelation, another option, potentially advantageous from an implementation point of view, is to make use of the fact that when the crosscorrelation function $\gamma_{\text{CRS}}(t')$ reaches a maximum, its Hilbert transform $\check{\gamma}_{\text{CRS}}(t')$ passes through zero [36]. This property implies that the phase of the crosscorrelation function's analytic form $\hat{\gamma}_{\text{CRS}}(t')$, defined as

$$\hat{\gamma}_{\text{CRS}}(t') = \gamma_{\text{CRS}}(t') - j\check{\gamma}_{\text{CRS}}(t') = |\hat{\gamma}_{\text{CRS}}(t')|e^{j\theta_{\text{CRS}}(t')} \quad (41)$$

is also zero when the crosscorrelation $\gamma_{\text{CRS}}(t')$ reaches a maximum. An experimental illustration of these properties is shown in Fig. 6, which plots the crosscorrelation as well as its Hilbert transform and phase for a pair of RF pulse returns from the input data used to generate Figs. 1 and 2. Hence, the time delay $t'_0 = -2vT_s/c$ between the two successive RF pulse returns defined by (36) can be identified by searching for zero-crossings of the phase $\theta_{\text{CRS}}(t')$. Provided that this is a linear function of time, it can be defined in terms of just two values, say at $t' = 0$ and $t' = t_s$, according to

$$\theta_{\text{CRS}}(t') = \theta_{\text{CRS}}(0) + [\theta_{\text{CRS}}(t_s) - \theta_{\text{CRS}}(0)] \frac{t'}{t_s} \quad (42)$$

Solving for the argument t_0 which results in $\theta_{\text{CRS}}(t_0) = 0$, gives

$$t'_0 = -\frac{\theta_{\text{CRS}}(0)t_s}{\theta_{\text{CRS}}(t_s) - \theta_{\text{CRS}}(0)} \quad (43)$$

and, by making use of (40), the corresponding velocity estimate could be written as

$$v = \frac{c}{2} \frac{\theta_{\text{CRS}}(0)/2\pi T_s}{[\theta_{\text{CRS}}(t_s) - \theta_{\text{CRS}}(0)]/2\pi t_s} \quad (44)$$

This equation has some interesting implications. First, due to (39) and the fact that the autocorrelation and spectrum of a signal form a Fourier transform pair, the quantity $[\theta_{\text{CRS}}(t_s) - \theta_{\text{CRS}}(0)]/2\pi t_s$ in the denominator of (44) (i.e., the rate of change in phase along the fast-time axis) provides an estimate of the RF signal's central frequency f_{RFC} . Then, because of the mathematical equivalence between the autocorrelation of the analytic signal and the analytic form of the autocorrelation function [37, ch. 10.4], the quantity $\theta_{\text{CRS}}(0)/2\pi T_s$ in the numerator of (44) (i.e., the rate of phase change along the slow-time axis) is identical to the Doppler frequency estimate provided by the 2D autocorrelator in (13). Therefore, (44) can be expressed as $v = (c/2)(F_D/f_{\text{RFC}})$, which is effectively a full evaluation of the Doppler equation and equivalent to the estimate provided by the 2D autocorrelator (see (15)). At this point it should be emphasized that, while the preceding material highlights the fundamental similarities between the crosscorrelation and 2D autocorrelation approaches for axial velocity estimation, the two approaches have been shown to be mathematically equivalent for the specific set of conditions mentioned above (namely, the ideal time-shift model of expression 36 and the linear phase model of expression 42). Consequently, no firm statements can be made when one or more of those conditions is not valid (e.g., when the linear phase assumption is violated because of phase discontinuities in the RF signal, due to destructive interference [38]).

When more than one time shift (or velocity component) is present in the RF returns, i.e.

$$r^a(t, n+1) = \sum_k r_k^a\left(t + \frac{2v_k T_s}{c}, n\right) \quad (45)$$

it is still straightforward to show that

$$\gamma_{\text{CRS}}(t') = \sum_k \gamma\left(t' + \frac{2v_k T_s}{c}\right) \quad (46)$$

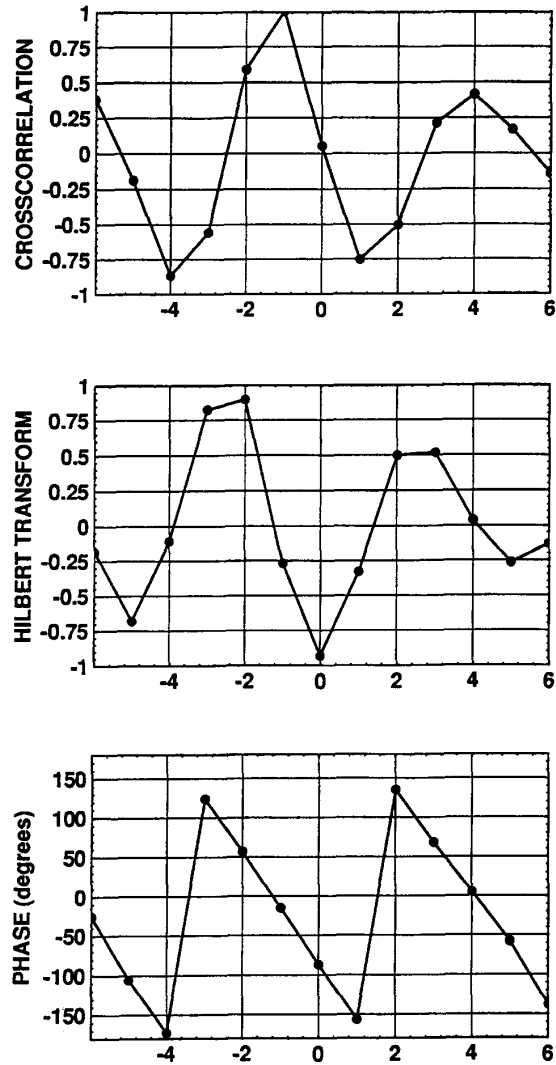


Fig. 6. Crosscorrelation between two successive RF pulse returns (top) as well as its Hilbert transform (middle) and phase (bottom) for a range gate length of 20 RF samples (the sampling RF interval is 50 ns). Note that the true shift between the two RF returns, which were taken from the moving-belt data first used in Fig. 1, is 65 ns.

where it has been assumed that the individual returns $r_k^a(t, n)$ associated with each velocity component share the same autocorrelation function $\gamma(t')$. In this case, however, the equivalent of (40) cannot be derived without knowing the exact form of $\gamma(t')$. In other words, it is not possible to show theoretically that the maximum of the crosscorrelation function occurs at a time related to the mean velocity, although this property has been verified experimentally [8], [10].

Turning now to the implementation of the crosscorrelator for discrete signals, the following crosscorrelation formula applies:

$$\gamma_{\text{CRS}}(m') = \sum_{m=0}^{M-m'-1} r(m, n)r(m+m', n+1) \quad (47)$$

This is a sampled finite-extent version of (37). In general, the position of the crosscorrelation maximum does not coincide with the sampling grid and has to be found in terms of an interpolation scheme. The underlying idea is, first, to locate the peak of the sampled crosscorrelation function (coarse estimate) and, then, fit a curve which approximates the shape of the crosscorrelation around its maximum (fine estimate). A parabola is the most common choice for the fitting curve. According to this method [39], if l_{coarse} denotes the index which corresponds to the crosscorrelation peak, the fractional value which defines the global maximum is given by (48) while the mean velocity is then calculated from

$$\langle v_{\text{CRS}} \rangle = -\frac{ct_s l_{\text{fine}}}{2T_s} \quad (49)$$

From the theoretical expressions for the statistical properties of the crosscorrelator which have been derived in [40], it can be stated that the standard deviation of the estimator's output is:

- independent of the time shift
- proportional to the RF sampling interval t_s .
- dependent on a function of $1 + 1/\text{SNR}$
- inversely proportional to the square root \sqrt{M} of the number of samples used in evaluating the crosscorrelation function.
- inversely proportional to the bandwidth of the RF signal.

These statements are applicable to the case of an ideal time-shift relationship, where each pulse return is an identical but delayed version of its predecessors. A detailed study of the crosscorrelator's performance in the context of ultrasonic measurement of flow, which included error analysis and computer simulations, has shown that the standard deviation of this estimator is inversely proportional to the maximum correlation coefficient between two consecutive RF returns [7]. The maximum correlation coefficient is, in turn, determined by the lateral beamwidth and transverse velocity magnitude as well as by the number of velocity components present within the range cell [7]. Another factor that affects the performance of the crosscorrelator is the extent of the search region [41]. This is particularly true for low SNRs, where expanding the search region results in a sharp increase in the number of false peaks found [42]. In the implementation adopted here, the argument m' of the crosscorrelation function could take values in the range

$$m' = \left\{ -1 - \frac{1}{2f_c}, -\frac{1}{2f_c}, \dots, 0, \dots, \frac{1}{2f_c}, \frac{1}{2f_c} + 1 \right\} \quad (50)$$

where $1/f_c$ denotes the normalized period of the central frequency component. The search region for the crosscorrelation peak was restricted to plus/minus half the normalized central period $1/2f_c$, while the two extreme points on either side of the range in (50) were evaluated in case they were needed for the parabolic fit operation of (48). A sequence of axial

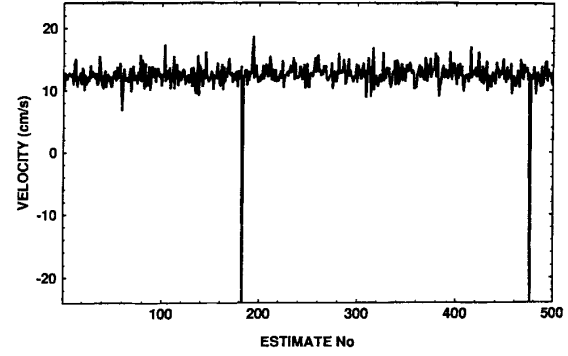


Fig. 7. Sequence of axial velocity estimates provided by the crosscorrelator. The input data set for this figure was the same as the one used in Figs. 2 and 4.

velocity estimates provided by the crosscorrelator, based on the same RF data and range gate length as those used in Figs. 2 and 4, is shown in Fig. 7. Comparison with the estimates of the 2D autocorrelator (Fig. 2) indicates that the outputs of both estimators are very similar (with the exception of two false negative peaks in the crosscorrelator's case) and clearly superior to the output of the conventional 1D autocorrelator (Fig. 4).

The preceding discussion is applicable to the crosscorrelator when only a pair of RF returns is used. The question arises as to how this estimator can be modified to handle an arbitrary number of RF returns. It has been proposed in [8] that $N(N-1)/2$ individual shift estimates can be obtained by operating on all possible pairs which are separated by $1, 2, \dots, N-1$ pulse repetition intervals T_s . These estimates can then be combined according to a weighted averaging scheme with experimentally determined weights. However, recent *in vitro* experiments suggest that this weighted averaging scheme does not appear to improve the precision of the estimates, compared to straight averaging applied to the $N-1$ consecutive pairs of RF returns [10]. In this paper, and as part of the simulations described in Sections III and IV, we evaluated the latter approach as well as an alternative which incorporates all RF returns into a single crosscorrelation function

$$\gamma_{\text{CRS}}(m') = \sum_{n=0}^{N-2} \sum_{m=0}^{M-m'-1} r(m, n) r(m+m', n+1) \quad (51)$$

Since the results obtained from (51) were considerably better, they were selected for presentation in Section IV. The main reason for the superiority of (51) is that the search for the crosscorrelation maximum is carried out on the average of the individual crosscorrelation functions obtained from consecutive pairs of RF returns, thus minimizing the occurrence of false peaks.

To complete the description of the crosscorrelator, two groups of related techniques will be briefly discussed. The first

$$l_{\text{fine}} = \frac{1}{2} \frac{\gamma_{\text{CRS}}(l_{\text{coarse}} - 1) - \gamma_{\text{CRS}}(l_{\text{coarse}} + 1)}{\gamma_{\text{CRS}}(l_{\text{coarse}} - 1) - 2\gamma_{\text{CRS}}(l_{\text{coarse}}) + \gamma_{\text{CRS}}(l_{\text{coarse}} + 1)} + l_{\text{coarse}} \quad (48)$$

is a family of estimators known as generalized crosscorrelation functions [43]. The basic concept behind this approach is to prefilter the RF signals to make them as white as possible and, therefore, increase the height and decrease the width of the primary crosscorrelation peak. Simulations have shown that this approach offers performance gains only when the exact spectra of the signals involved are known [44]. This is clearly not the case in color flow mapping. The second group attempts to find the best match between consecutive pairs of signals by searching for the shift that minimizes the sum of either the squared or absolute differences. It has been shown in [40] that both techniques are identical to the crosscorrelator, with the exception of very high SNRs (>20 dB) where they exhibit slightly better performance, although these findings are contradicted by other studies [45] which suggest that the crosscorrelator is consistently better. In any case, difference techniques offer a clear implementation advantage because of their relative computational simplicity, as demonstrated by a hardware version of the sum-of-absolute-differences estimator which has been incorporated into a real-time speckle-tracking system for quantifying two-dimensional motion (axial and lateral velocity components) [46].

III. SIMULATION DETAILS

The aim of the simulation was to generate data which would reproduce the stochastic properties of real-world signals in a computationally efficient manner, so that reliable statistics could be drawn on the performance of the velocity estimators under investigation by carrying out a large number of repetitions.

A. RF Pulse

To generate an asymmetric RF pulse, which resembles real signals more closely than the common choice of a Gaussian-shaped pulse, the discrete equivalent of a model suggested in [47] was used:

$$\begin{aligned} s(m) &= (a_1 m + a_2 m^2) e^{-bm} \cos(2\pi f_c m) \\ m &= 0, 1, \dots, 511 \\ f_c &= 1/8 \end{aligned} \quad (52)$$

Note that the normalized central pulse frequency f_c was always set to one eighth (corresponding to a sampling rate equal to eight times the pulse's central frequency) to permit a proper implementation of the crosscorrelator, whose performance was observed to deteriorate for lower sampling rates. The other parameters (a_1, a_2 and b) in (52) were varied to achieve the desired pulse characteristics (20-dB length and/or 20-dB fractional bandwidth).

B. Backscattered Signal

The simulation of the backscattered RF signal adopted the model of expression (4), which describes scatterers arranged in concentric annulae sharing the same axis as the ultrasound beam and moving towards the transducer with different velocities (i.e., axial flow in the presence of multiple velocity components). The starting point was to generate K sequences

of 512 points, corresponding to K velocity components, by convolving the pulse sequence $s(m)$ of (52) with white Gaussian noise $g(m, k)$

$$\begin{aligned} r_k(m, k) &= s(m) * g(m, k) \\ m &= 0, 1, \dots, 511 \\ k &= 0, 1, \dots, K-1 \end{aligned} \quad (53)$$

The convolution was performed in the frequency domain by multiplying the row-wise complex Fourier transforms of $s(m)$ and $g(m, k)$ and then evaluating the inverse Fourier transform of the product. Approximating the interaction between the pulse and a very large number of discrete scatterers by means of the operation described above can be justified on the basis of the central-limit theorem [37, ch. 8.6]. Shifting of the individual returns $r_k(m, k)$ was achieved by means of an interpolation scheme described in [13]. The exact formula used to calculate the backscattered RF array $r(m, n)$ was

$$\begin{aligned} r(m, n) &= \frac{1}{K} \sum_{k=0}^{K-1} \{ r_k([m_k], k) \cos[2\pi(m_k - [m_k])] \\ &\quad + r_k([m_k] + 1, k) \sin[2\pi(m_k - [m_k])] \} \end{aligned} \quad (54)$$

where $m_k = m + (2nv_k T_s / ct_s)$ and $[m_k]$ denotes the integer part of m_k . In all cases, thirty three velocity components were chosen ($K = 33$). In order to evaluate the effect of velocity spread on the estimators' performance, individual velocities v_k were distributed uniformly around the mean velocity $\langle v \rangle$ with the two extreme velocity spread cases considered being 0% (all v_k values equal to $\langle v \rangle$) and 50% (v_k values covering the range $[0.75\langle v \rangle, 1.25\langle v \rangle]$).

The analytic RF signal $\hat{r}(m, n)$ was calculated from $r(m, n)$ with the help of (8). In practical terms, this involved evaluating the row-wise complex Fourier transform of $r(m, n)$, setting its negative-frequency part to zero and then performing the inverse Fourier transform. The demodulated I & Q signal $z(m, n)$ was obtained by making use of (17), i.e. the row-wise complex Fourier transform of $\hat{r}(m, n)$ was shifted by f_c towards the origin of the frequency axis, followed by an inverse Fourier transform operation. We have verified that this approach produces results identical to those obtained by the conventional demodulation method (mixing with the reference complex sinusoid, followed by low-pass filtering).

C. Noise

Noise was added to the final RF signal $r(m, n)$, before calculating its analytic and demodulated versions. The noise array consisted of a number of rows equal to the ensemble length, each 512-samples long, of zero-mean white Gaussian samples which underwent row-wise filtering in the frequency domain using a rectangular bandpass function whose width was equal to the 20-dB fractional bandwidth of the transmitted RF pulse. In other words, it was implicitly assumed that, prior to velocity estimation, all energy of the backscattered signal outside the pulse bandwidth is suppressed. The SNR was then defined as the power of the signal array over the corresponding value of the noise array.

D. Velocity Estimators

All estimators were implemented in floating-point arithmetic. The crosscorrelator was applied to the RF signal $r(m, n)$ by means of (48)–(51). The 1D autocorrelator was applied to the integrated I & Q signal $z_{\text{int}}(n)$ using (28). The 2D autocorrelator was applied to the demodulated I & Q signal $z(m, n)$ using (20). In addition, to investigate the contribution of the explicit mean RF frequency estimation in the overall performance of the 2D autocorrelator, a simplified version (denoted as 2D_DOP) which retained only the Doppler estimation part of the 2D autocorrelator was implemented according to (55).

E. Output Statistics

The results of the following section were based on the standard deviation of the estimators' output, which determines the precision of each technique. Individual standard deviation values were derived from 16384 repetitions for each combination of simulation parameters. Such a high number of repetitions was required in order to obtain reliable statistics, due to the noisy nature of the estimators under typical color flow mapping conditions. The estimators' accuracy was also documented, but was not included in the results presented in the following section because none of the techniques suffered from significant systematic bias for the conditions considered by the simulation studies. Differences between the true and estimated means did occur at low SNRs, but this was due to the presence of "spikes" in the estimators' output (this term refers to grossly inaccurate estimates, as opposed to "jitter" that refers to random fluctuations around the true mean) rather than a manifestation of systematic error.

IV. RESULTS

From the description of the individual estimators in Section II, it should be clear that their performance is determined by a number of factors which encompass operating parameters and signal characteristics (range gate length, ensemble length, pulse length or—equivalently—fractional transmitted bandwidth, noise level, mean velocity and velocity spread). Obviously, it is impossible to scan the entire multidimensional space defined by all these factors. Our approach was to establish a few reference points in the multidimensional space and then slice the space with planes (velocity spread versus factor under investigation) passing through the reference points. The following conventions were adopted.

- Instead of velocities, the estimators were used to calculate the mean target shift (displacement) between successive pulse emissions. All the simulation results reported here were based on fixed true mean shift equal to 0.25 wavelengths of the pulse's central frequency component. The simulations were also repeated for true shifts covering the full nonaliased range (0.0–0.5 wavelengths), but those results are not presented here due to space limitations.
- To investigate the effect of velocity spread, in all cases examined the spread of individual shifts around the true mean shift was varied from 0–50% in six equally-spaced steps (i.e., individual shifts uniformly distributed in the range 0%, $\pm 5\%$, $\pm 10\%$, $\pm 15\%$, $\pm 20\%$ and $\pm 25\%$ of the true mean shift).
- The performance of the estimators was characterized in terms of their precision, which was defined as the standard deviation of their output expressed as a percentage of the true mean shift. In all cases, precision graphs were formed for each estimator using dash (crosscorrelator), dot (1D autocorrelator), solid (2D autocorrelator) and dash/dot (2D_DOP autocorrelator, the Doppler-only version of the 2D autocorrelator defined in (55)) curves. Graphs documenting the effect of a particular factor were placed side-by-side to allow trends to be more easily appreciated.

A. Range Gate Length

The precision of the estimators under investigation is plotted as a function of the shift spread in Fig. 8 for range gate lengths equal to 1, 3, 5, 7, and 9 wavelengths of the pulse's central frequency component. The fixed simulation parameters for this figure were: 20-dB fractional transmitted bandwidth of 0.75 (the corresponding 20-dB pulse length was 5.2 wavelengths); SNR of 20 dB; ensemble of 8 pulses.

From the graphs of Fig. 8, it is apparent that all estimators benefit from longer range gates, with improvement factors which depend on somewhere between the square- and cubic-root of the fractional increase in the range gate length. At the same time, the precision curves of all estimators exhibit an almost linear deterioration as the shift spread becomes higher. This pattern suggests that in a real-world nonaxial flow situation where—unlike the present simulation set-up which models axial flow—extending the range gate results in a higher velocity spread, the benefits of a longer range gate would be partially offset by the deterioration due to the presence of multiple velocity components. Consequently, the optimum range gate length would depend on a combination of factors

$$\langle v_{2D_DOP} \rangle = \frac{c}{2} \frac{\frac{1}{2\pi T_s} \tan^{-1} \left\{ \frac{\sum_{m=0}^{M-1} \sum_{n=0}^{N-2} [Q(m, n)I(m, n+1) - I(m, n)Q(m, n+1)]}{\sum_{m=0}^{M-1} \sum_{n=0}^{N-2} [I(m, n)I(m, n+1) + Q(m, n)Q(m, n+1)]} \right\}}{f_{\text{dem}} t_s} \quad (55)$$

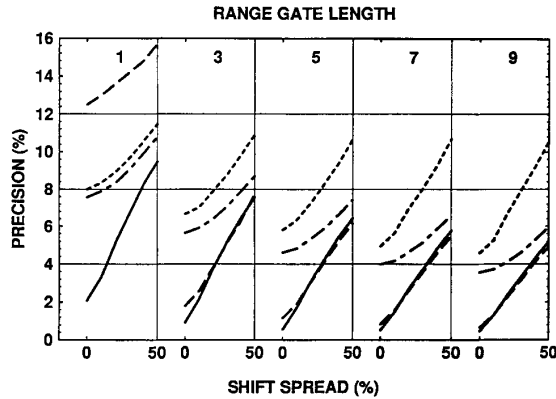


Fig. 8. Precision of the crosscorrelator, 1D, 2D_DOP and 2D autocorrelator (dash, dot, dash/dot and solid curves, respectively) versus the shift spread (individual shifts uniformly distributed in the range $\pm 0, 5, 10, 15, 20$ and 25% of the true mean shift of 0.25λ), for range gates of 1, 3, 5, 7 and 9λ . The simulations were carried out using a 20-dB fractional bandwidth of 0.75, SNR of 20 dB and ensemble of 8 pulses.

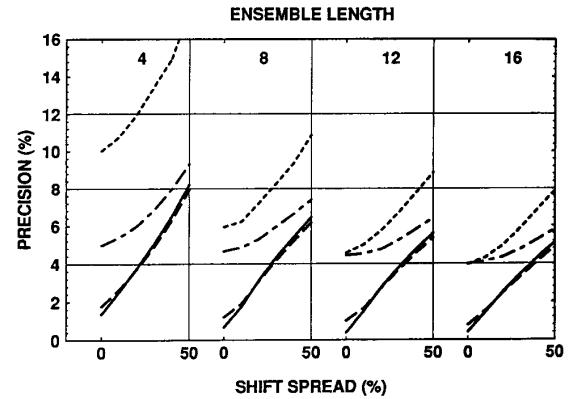


Fig. 9. Precision of the crosscorrelator, 1D, 2D_DOP and 2D autocorrelator (dash, dot, dash/dot and solid curves, respectively) versus the shift spread (individual shifts uniformly distributed in the range $\pm 0, 5, 10, 15, 20$ and 25% of the true mean shift of 0.25λ), for ensembles of 4, 8, 12 and 16 pulses. The simulations were carried out using a 20-dB fractional bandwidth of 0.75, SNR of 20 dB and range gate of 5λ .

such as the shear rate, angle of insonation, lateral beamwidth and scan plane thickness.

As far as performance comparisons between the different estimators are concerned, the 2D autocorrelator and crosscorrelator differ significantly only for the case of a range gate equal to one wavelength. The poor precision of the crosscorrelator for this case, which is caused by spikes rather than jitter, suggests that this estimator is associated with a high probability of false peaks for very short range gates. However, for all other cases, the 2D autocorrelator and crosscorrelator are nearly identical and clearly superior to the 1D autocorrelator. For example, the 2D autocorrelator and crosscorrelator can achieve better precision for a range gate of 3 wavelengths than the 1D autocorrelator for a range gate of 9 wavelengths.

An insight into the source of performance gains for the 2D autocorrelator can be obtained by comparing its precision curves with those of the 2D_DOP and 1D estimators. The consistently better performance of the 2D_DOP autocorrelator in comparison with the 1D autocorrelator indicates that the 2D form of Doppler estimation (frequency averaging along both the depth and ensemble directions) is always superior to 1D Doppler estimation (filtering of the I & Q signal along the depth direction followed by frequency averaging only along the ensemble direction). At the same time, the gradual convergence of the 2D and 2D_DOP autocorrelator as the shift spread becomes higher reveals that the explicit estimation of the mean RF frequency performed by the 2D autocorrelator is highly beneficial as long as there is no significant velocity spread, which tends to weaken the correlation between the mean Doppler and RF frequencies.

B. Ensemble Length

Fig. 9 plots the precision of the estimators under investigation as a function of the shift spread for ensembles equal to 4, 8, 12, and 16 pulses. The fixed simulation parameters for this figure were: 20-dB fractional transmitted bandwidth of 0.75

(the corresponding 20-dB pulse length was 5.2 wavelengths); SNR of 20 dB; range gate length of 5 wavelengths.

The precision curves of Fig. 9 exhibit the expected square-root dependence on the ensemble length as well as the almost linear deterioration as the shift spread becomes higher, originally observed in the previous subsection. Again, the 2D autocorrelator and crosscorrelator are nearly identical and outperform the 1D autocorrelator by a significant margin. For example, the precision curves of the 2D autocorrelator and crosscorrelator for an ensemble of 4 pulses are better than the precision curve of the 1D autocorrelator for 16 pulses. The margin, however, decreases gradually for longer ensembles. This pattern is another manifestation of the fact that the 1D autocorrelator performs frequency averaging only along the ensemble direction and, therefore, requires a large number of pulses to achieve satisfactory performance.

C. Signal-to-Noise Ratio

The effect of noise on the performance of the estimators under investigation is documented in Fig. 10, which plots their precision as a function of the shift spread for SNRs of 20, 15, 10, 5 and 0 dB. The fixed simulation parameters for this figure were: 20-dB fractional transmitted bandwidth of 0.75 (the corresponding 20-dB pulse length was 5.2 wavelengths); range gate of 5 wavelengths; ensemble of 8 pulses.

From the precision curves of Fig. 10 it can be readily seen that the 1D autocorrelator exhibits the highest sensitivity to noise, which becomes quite significant for SNRs < 10 dB. The precision curves of the 2D autocorrelator and crosscorrelator are barely indistinguishable for SNRs ≥ 10 dB, but the performance of the crosscorrelator deteriorates noticeably for lower SNRs indicating a reduced robustness to noise. Finally, it is interesting to note that the superiority of the 2D autocorrelator over its simplified Doppler-only counterpart (2D_DOP estimator) is gradually reduced as the SNR becomes poorer. This trend implies that the Doppler and RF frequency

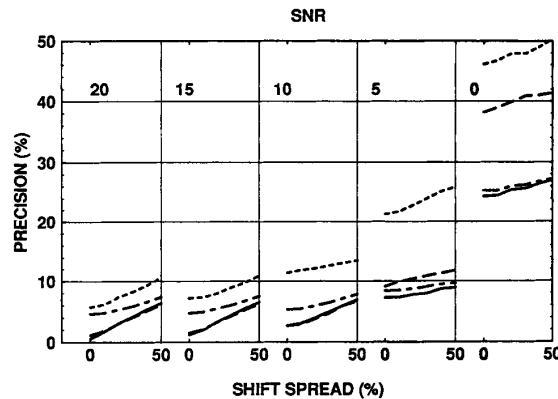


Fig. 10. Precision of the crosscorrelator, 1D, 2D_DOP and 2D autocorrelator (dash, dot, dash/dot and solid curves, respectively) versus the shift spread (individual shifts uniformly distributed in the range $\pm 0, 5, 10, 15, 20$ and 25% of the true mean shift of 0.25λ), for SNRs of 20, 15, 10, 5 and 0 dB. The simulations were carried out using a 20-dB fractional bandwidth of 0.75, range gate of 5λ and ensemble of 8 pulses.

fluctuations do not track each other closely in the presence of heavy noise and, therefore, under those circumstances the precision benefits offered by the RF estimation part of the 2D autocorrelator become marginal.

D. Pulse Bandwidth

Fig. 11 documents the effect of the transmitted pulse bandwidth on the estimators' precision in the presence of low and high noise. The simulations were designed to achieve constant axial resolution by considering four 20-dB fractional bandwidths (0.50, 0.75, 1.00 and 1.25) and selecting the corresponding range gate lengths (2.2, 5.2, 5.8 and 6.3 wavelengths) so that in all four cases the 20-dB extent of the sample volume (measured by convolving the pulse envelope with the range gate) was equal to 8.5 wavelengths. The low- and high-noise levels were selected to achieve $\text{SNR} = 20$ and 0 dB for the narrowest bandwidth considered. The SNRs for the other three—increasingly broader—bandwidths were obviously poorer (18.2, 17.0, and 16.0 dB and $-1.8, -3.0$, and -4.0 dB for the low- and high-noise case, respectively, based on actual measurements) because the same amount of signal power was spread over a wider frequency range, while the noise level (power per unit of frequency) remained constant. In all cases, an ensemble of 8 pulses was used.

The results of Fig. 11 show that, under the specific conditions of this simulation, the 20-dB fractional bandwidth of 0.75 represents the optimum choice for the 1D autocorrelator. Based on the fact that the range gate corresponding to the optimum bandwidth was equal to the 20-dB pulse length for that bandwidth (5.2 wavelengths), it appears that the general PW Doppler guideline of matching the range gate to the pulse length [25] is also applicable to the 1D autocorrelator. Similar conclusions were reached by repeating the simulations with a variety of bandwidths and sample volume sizes. On the contrary, Fig. 11 shows that the performance of the 2D

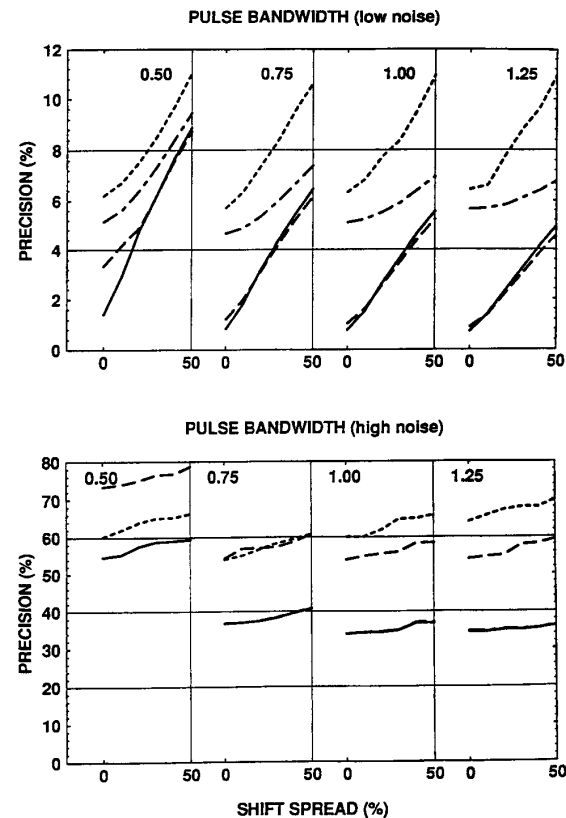


Fig. 11. (Top): Precision of the crosscorrelator, 1D, 2D_DOP and 2D autocorrelator (dash, dot, dash/dot and solid curves, respectively) versus the shift spread (individual shifts uniformly distributed in the range $\pm 0, 5, 10, 15, 20$ and 25% of the true mean shift of 0.25λ), for 20-dB fractional bandwidths of 0.50, 0.75, 1.00 and 1.25. The simulations were carried out using a fixed noise level which corresponds to $\text{SNR} = 20$ dB for the narrowest bandwidth considered and ensemble of 8 pulses. The range gate lengths were set equal to 2.2, 5.2, 5.8 and 6.3 λ , from left to right, so that the 20-dB length of the sample volume was equal to 8.5λ for all bandwidths. (Bottom): As above, with a fixed noise level which corresponds to $\text{SNR} = 0$ dB for the narrowest bandwidth considered.

autocorrelator and crosscorrelator continue to improve as the bandwidth becomes broader (and, hence, more depth samples can be used while maintaining the same axial resolution), indicating that for these techniques the gains offered by longer range gates can overcome the losses due to poorer SNRs.

Apart from the different trade-offs associated with each estimator when both the transmitted pulse bandwidth and the range gate length are adjusted to achieve a constant sample volume size, Fig. 11 provides confirmation for some observations made in previous subsections. More specifically, it is clear that the 2D autocorrelator is almost identical to the crosscorrelator for high SNRs, but exhibits increased robustness under heavy noise conditions. Also, the fact that the precision curves of the 2D and 2D_DOP autocorrelators in the bottom part of Fig. 11 are indistinguishable demonstrates that the presence of heavy noise disrupts the correlation between Doppler and RF frequencies.

V. CONCLUDING REMARKS

This paper has examined a novel technique, referred to as the 2D autocorrelator, which derives the mean axial velocity at each location of the range gate by estimating both the Doppler and RF mean frequencies—in other words by performing a full evaluation of the Doppler equation. In addition to a description of the 2D autocorrelator, two other established velocity estimators were studied: the conventional 1D autocorrelator, as a representative of phase-domain techniques and because it is the standard color flow mapping method in commercial scanners, and the crosscorrelator, as a representative of time-domain techniques and because a simpler form of it (1-bit crosscorrelation) has been commercially adopted [6], [23]. Section II described all three estimators in a unifying manner, and highlighted similarities and differences.

In brief, it was shown that the 1D autocorrelator derives a mean Doppler frequency estimate which is mathematically equivalent to the centroid of the measured 2D (Doppler versus RF frequency) spectrum at the column corresponding to the RF sinusoid used in the demodulation process, while the 2D autocorrelator evaluates the mean Doppler frequency based on the entire 2D spectrum. Alternatively, and in more practical terms, the two estimators can be thought of as following different averaging strategies for Doppler estimation; the 1D autocorrelator averages the frequency estimates along the ensemble axis only, since the information along the depth axis is used solely for filtering purposes, while the 2D autocorrelator performs frequency averaging along both directions. A second difference is that, unlike the 1D autocorrelator, the 2D autocorrelator performs explicit estimation of the mean RF frequency of the data inside the range gate and, therefore, can reduce the variance of the velocity estimates by compensating for the random RF frequency fluctuations which cause similar fluctuations in the Doppler frequency. The simulations results of Section IV showed that the RF estimation part of the 2D autocorrelator offers substantial benefits for signals with modest velocity spread and good SNR, but these benefits become marginal in the presence of significant velocity spreads and/or heavy noise, which weaken the correlation between Doppler and RF fluctuations. Apart from improving the precision of velocity measurements, explicit estimation of the mean RF frequency can potentially overcome the bias effect that frequency-dependent attenuation has on the 1D autocorrelator [48]. This topic is briefly addressed in the experimental companion to this paper [49].

The material of Section II also showed that the 2D autocorrelator and the crosscorrelator share a number of common features. Both estimators are explicitly based on the same model (the gradual translation of the backscattered echoes with respect to previous pulse transmissions, due to the changing distance between the transducer and groups of moving scatterers) and make extensive use of the information along the depth direction. It was also shown that, under a set of specific conditions (a single velocity component and a backscattered signal whose phase does not exhibit discontinuities), the two estimators are mathematically equivalent.

The performance of the three velocity estimators was assessed by means of extensive simulations which documented the effect of the velocity spread, range gate length, ensemble length, noise level and transmitted bandwidth on estimation precision. In summary, the 1D autocorrelator was found to be consistently inferior to the other two estimators examined here, with particularly poor performance for short ensembles and low SNRs. It was also noted that among the various combinations of pulse and range gate lengths which result in the same axial resolution, matching the range gate to the pulse length represents the optimum choice for the 1D autocorrelator. As far as the 2D autocorrelator and crosscorrelator are concerned, it was repeatedly observed that they were almost identical under low-noise conditions, but the 2D autocorrelator was shown to offer noticeably better robustness in the presence of heavy noise. The 2D autocorrelator is further examined, on an experimental basis, in the companion to this paper [49].

Based on the fact that the 2D autocorrelator and the crosscorrelator rely on the full 2D data set of backscattered echoes and produce comparable results, we postulate that the primary factor in predicting the performance of a velocity estimator is the information content of the input signal. This statement does not imply that all estimators applied to the same input will produce identical results; simply that, when estimators are grouped together on the basis of their performance, the type of input data is the most relevant criterion. Under these circumstances, practical issues such as the sampling rate or the number of operations per estimate become perhaps more important than minor performance differences. From this point of view, the proposed estimator appears to represent a favorable option, since it can be applied to the demodulated (baseband) signal and requires evaluation of only two lags of the 2D autocorrelation function.

APPENDIX A

Assuming that the analytic-form array $\hat{r}(m, n)$ has a size of $M \times N$ ($m = 0, 1, \dots, M-1$ and $n = 0, 1, \dots, N-1$), its autocorrelation function is given by

$$\hat{\gamma}(m', n') = \sum_{m=0}^{M-m'-1} \sum_{n=0}^{N-n'-1} \hat{r}(m, n) \hat{r}^*(m+m', n+n') \quad (A1)$$

The 2D autocorrelation function is also the inverse 2D Fourier transform of the power spectrum.

$$\hat{\gamma}(m', n') = \sum_{m=-M/2}^{M/2-1} \sum_{n=-N/2}^{N/2-1} \hat{\Gamma}\left(\frac{m}{M}, \frac{n}{N}\right) e^{j(2\pi m m' / M)} \cdot e^{j(2\pi n n' / N)} \quad (A2)$$

where $m/M, n/N$ correspond to the discrete normalized frequencies f and F , respectively.

Differentiation of (A2) with respect to the m' variable gives

$$\frac{\partial \hat{\gamma}(m', n')}{\partial m'} = \sum_{m=-M/2}^{M/2-1} \sum_{n=-N/2}^{N/2-1} j \frac{2\pi m}{M} \hat{\Gamma}\left(\frac{m}{M}, \frac{n}{N}\right) \cdot e^{j(2\pi m m' / M)} e^{j(2\pi n n' / N)} \quad (A3)$$

which, for $m' = n' = 0$, is equal to

$$\left. \frac{\partial \hat{\gamma}(m', n')}{\partial m'} \right|_{m'=n'=0} = \sum_{m=-M/2}^{M/2-1} \sum_{n=-N/2}^{N/2-1} j \frac{2\pi m}{M} \hat{\Gamma}\left(\frac{m}{M}, \frac{n}{N}\right) \quad (\text{A4})$$

By using (A4) and (A2) and taking into account the correspondence between $m/M, n/N$ and f, F , it is straightforward to verify that the following expression

$$\langle f \rangle = \frac{-j \frac{\partial \hat{\gamma}(m', n')}{\partial m'} \Big|_{m'=n'=0}}{\hat{\gamma}(0, 0)} \quad (\text{A5})$$

is the discrete equivalent of (9). This expression can be further simplified by taking into account the fact that the autocorrelation of a complex wide-stationary process is Hermitian [21, ch. 6.1], i.e.

$$\hat{\gamma}(m', n') = \hat{\gamma}^*(-m', -n') \quad (\text{A6})$$

By expressing the autocorrelation function in Cartesian and polar coordinates

$$\begin{aligned} \hat{\gamma}(m', n') &= \text{Re}[\hat{\gamma}(m', n')] + j \text{Im}[\hat{\gamma}(m', n')] \\ &= |\hat{\gamma}(m', n')| e^{j\theta(m', n')}. \end{aligned} \quad (\text{A7})$$

Equation (A6) implies that:

- The real part and magnitude $\text{Re}[\hat{\gamma}(m', n')]$, $|\hat{\gamma}(m', n')|$ are even functions of m', n' and therefore their partial derivatives at (0, 0) are equal to zero.
- The imaginary part and phase $\text{Im}[\hat{\gamma}(m', n')]$, $\theta(m', n')$ are odd functions of m', n' and therefore their values at (0, 0) are equal to zero.

Based on these properties, (A5) becomes

$$\langle f \rangle = \frac{1}{2\pi} \frac{\partial \theta(m', n')}{\partial m'} \Big|_{m'=n'=0} \quad (\text{A8})$$

which, for a small $m' \neq 0$, can be approximated by

$$\langle f \rangle \cong \frac{1}{2\pi} \frac{\theta(m', 0) - \theta(0, 0)}{m'} = \frac{1}{2\pi} \frac{\theta(m', 0)}{m'} \quad (\text{A9})$$

or, by using the smallest available lag value $m' = 1$

$$\langle f \rangle \cong \frac{1}{2\pi} \theta(1, 0) = \frac{1}{2\pi} \tan^{-1} \left\{ \frac{\text{Im}[\hat{\gamma}(1, 0)]}{\text{Re}[\hat{\gamma}(1, 0)]} \right\} \quad (\text{A10})$$

In a similar manner, it can be shown that the discrete equivalent of (10) can be approximated by

$$\langle F \rangle \cong \frac{1}{2\pi} \tan^{-1} \left\{ \frac{\text{Im}[\hat{\gamma}(0, 1)]}{\text{Re}[\hat{\gamma}(0, 1)]} \right\} \quad (\text{A11})$$

REFERENCES

- [1] P. N. T. Wells, "Physical and technical aspects of color flow ultrasound," in *Diagnostic Vascular Ultrasound*, K. H. Labs, K. A. Jager, D. E. Fitzgerald, J. P. Woodcock, and D. Neuerburg-Heusler, Eds. London: Edward Arnold, 1992, pp. 145–153.
- [2] C. Kasai, K. Namekawa, A. Koyano, and R. Omoto, "Real-time two-dimensional blood flow imaging using an autocorrelation technique," *IEEE Trans. Son. Ultrason.*, vol. SU-32, pp. 458–464, 1985.
- [3] D. H. Evans, W. N. McDicken, R. Skidmore, and J. P. Woodcock, *Doppler Ultrasound: Physics, Instrumentation and Clinical Applications*. Chichester: Wiley, 1989.
- [4] C. R. Deanne, F. Forsberg, N. Thomas, and V. C. Roberts, "Accuracy of color Doppler ultrasound velocity measurements in small vessels," *J. Biomed. Eng.*, vol. 13, pp. 249–254, 1991.
- [5] O. Bonnefous and P. Pesque, "Time-domain formulation of pulse Doppler ultrasound and blood velocity estimation by cross correlation," *Ultrason. Imag.*, vol. 8, pp. 73–85, 1986.
- [6] O. Bonnefous, P. Pesque, and X. Bernard, "A new velocity estimator for color flow mapping," in *Proc. IEEE Ultrason. Symp.*, 1986, pp. 885–860.
- [7] S. G. Foster, P. M. Embree, and W. D. O'Brien Jr., "Flow velocity profile via time domain correlation: error analysis and computer simulation," *IEEE Trans. Ultrason. Ferroelect. Freq. Cont.*, vol. 37, pp. 164–175, 1990.
- [8] P. M. Embree and W. D. O'Brien Jr., "Volumetric blood flow via time-domain correlation: Experimental verification," *IEEE Trans. Ultrason. Ferroelect. Freq. Cont.*, vol. 37, pp. 176–189, 1990.
- [9] I. A. Hein, J. T. Chen, W. K. Jenkins, and W. D. O'Brien Jr., "A real-time ultrasound time-domain correlation blood flowmeter: Part I—Theory and design," *IEEE Trans. Ultrason. Ferroelect. Freq. Cont.*, vol. 40, pp. 768–775, 1993.
- [10] I. A. Hein and W. D. O'Brien Jr., "A real-time ultrasound time-domain correlation blood flowmeter: Part II—Performance and experimental verification," *IEEE Trans. Ultrason. Ferroelect. Freq. Cont.*, vol. 40, pp. 776–785, 1993.
- [11] K. W. Ferrara and V. R. Algazi, "A new wideband spread target maximum likelihood estimator for blood flow velocity estimation—Part I: Theory," *IEEE Trans. Ultrason. Ferroelect. Freq. Cont.*, vol. 38, pp. 1–16, 1991.
- [12] —, "A new wideband spread target maximum likelihood estimator for blood flow velocity estimation—Part II: Evaluation of estimators," *IEEE Trans. Ultrason. Ferroelect. Freq. Cont.*, vol. 38, pp. 17–26, 1991.
- [13] P. G. M. De Jong, T. Arts, A. P. G. Hoeks, and R. S. Reneman, "Determination of tissue velocity by correlation interpolation of pulsed ultrasonic signals," *Ultrason. Imag.*, vol. 12, pp. 84–98, 1990.
- [14] —, "Experimental evaluation of the correlation interpolation technique to measure regional tissue velocity," *Ultrason. Imag.*, vol. 13, pp. 145–161, 1991.
- [15] A. P. G. Hoeks, T. G. J. Arts, P. J. Brands, and R. S. Reneman, "Comparison of the performance of the RF cross correlation and Doppler autocorrelation technique to estimate the mean velocity of simulated ultrasound signals," *Ultrasound Med. Biol.*, vol. 19, pp. 727–740, 1993.
- [16] I. A. Hein and W. D. O'Brien Jr., "Current time-domain methods for assessing tissue motion by analysis of reflected ultrasound echoes—A review," *IEEE Trans. Ultrason. Ferroelect. Freq. Cont.*, vol. 40, pp. 84–102, 1993.
- [17] W. T. Mayo and P. M. Embree, U.S. Patent Number 4930513, June 5, 1990.
- [18] L. S. Wilson, "Description of broad-band pulsed Doppler ultrasound processing using the two-dimensional Fourier transform," *Ultrason. Imag.*, vol. 13, pp. 301–315, 1991.
- [19] T. Loupas and R. W. Gill, "Multi-frequency Doppler: Improving the quality of spectral estimation by making full use of the information present in the backscattered RF echoes," *IEEE Trans. Ultrason. Ferroelect. Freq. Cont.*, vol. 41, pp. 522–531, 1994.
- [20] O. Bonnefous, "Time domain color flow imaging: Methods and benefits compared to Doppler," *Acoustical Imag.*, vol. 19, pp. 301–309, 1992.
- [21] J. S. Lim, *Two-dimensional Signal and Image Processing*. Englewood Cliffs: Prentice Hall, 1990.
- [22] R. Bracewell, *The Fourier Transform and its Applications*. New-York: McGraw-Hill, 1965.
- [23] D. W. Riekey, R. Rankin, and A. Fenster, "A velocity evaluation phantom for color and pulsed Doppler instruments," *Ultrasound Med. Biol.*, vol. 18, pp. 479–494, 1992.
- [24] J. G. Proakis and D. G. Manolakis, *Introduction to Digital Signal Processing*. New York: Macmillan, 1988.
- [25] K. Kristoffersen, "Optimal receiver filtering in pulsed Doppler ultrasound blood velocity measurements," *IEEE Trans. Ultrason. Ferroelect.*

- Freq. Cont.*, vol. 33, pp. 51–58, 1986.
- [26] G. T. Herman, *Image Reconstruction from Projections*. New York: Academic Press, 1980.
 - [27] K. S. Miller and M. M. Rochwarger, "A covariance approach to spectral moment estimation," *IEEE Trans. Inform. Theory*, vol. IT-18, pp. 588–596, 1972.
 - [28] D. S. Zrnic, "Spectral moment estimates from correlated pulse pairs," *IEEE Trans. Aerospace Elect. Syst.*, vol. 13, pp. 344–354, 1977.
 - [29] G. H. Leeuwen, A. P. G. Hoeks, and R. S. Reneman, "Simulation of real-time frequency estimators for pulsed Doppler systems," *Ultrason. Imag.*, vol. 8, pp. 252–271, 1986.
 - [30] K. Kristoffersen, "Time domain estimation of the center frequency and spread of the Doppler spectra in diagnostic ultrasound," *IEEE Trans. Ultrason. Ferroelect. Freq. Cont.*, vol. 35, pp. 685–700, 1988.
 - [31] A. Herment, G. Demoment, J. P. Guglielmi, Ph. Dumeé, and C. Pellot, "Adaptive estimation of the mean frequency of a Doppler signal from short data windows," *Ultrasound Med. Biol.*, vol. 9, pp. 901–919, 1991.
 - [32] T. Loupas and W. N. McDicken, "Low-order complex AR models for mean and maximum frequency estimation in the context of color flow mapping," *IEEE Trans. Ultrason. Ferroelect. Freq. Cont.*, vol. 37, pp. 890–901, 1990.
 - [33] Y. B. A. Ahn and B. P. Song, "Estimation of mean frequency and variance of ultrasonic Doppler signal by using second-order autoregressive model," *IEEE Trans. Ultrason. Ferroelect. Freq. Cont.*, vol. 38, pp. 172–182, 1991.
 - [34] J. S. Bendat and A. G. Piersol, *Engineering Applications of Correlation and Spectral Analysis*. New York: Wiley, 1980.
 - [35] Special Issue on Time Delay Estimation, *IEEE Trans. Acoust. Speech Signal Processing*, vol. 29, no. 3, Part II, Jun. 1981.
 - [36] R. C. Cabot, "A note on the application of Hilbert transform to time delay estimation," *IEEE Trans. Acoust. Speech Signal Processing*, vol. ASSP-29, pp. 607–609, 1981.
 - [37] A. Papoulis, *Probability, Random Variables and Stochastic Processes*. Tokyo: McGraw-Hill, 1981.
 - [38] D. A. Seggie and S. Leeman, "Deterministic approach towards ultrasound speckle reduction," *IEE Proc.—Part A*, vol. 134, pp. 188–192, 1987.
 - [39] R. Moddemeijer, "On the determination of position of extrema of sampled correlators," *IEEE Trans. Signal Processing*, vol. 39, pp. 217–219, 1991.
 - [40] G. Jacovitti and G. Scarano, "Discrete time techniques for time delay estimation," *IEEE Trans. Signal Processing*, vol. 41, pp. 525–533, 1993.
 - [41] J. A. Jensen, "Range/velocity limitations for time-domain blood velocity estimation," *Ultrasound Med. Biol.*, vol. 19, pp. 741–749, 1993.
 - [42] J. P. Ianniello, "Time delay estimation via cross-correlation in the presence of large estimation errors," *IEEE Trans. Acoust. Speech Signal Processing*, vol. ASSP-30, pp. 998–1003, 1982.
 - [43] G. C. Carter, "Coherence and time delay estimation," *Proc. IEEE*, vol. 75, pp. 236–255, 1987.
 - [44] K. Scarbrough, N. Ahmed, and G. C. Carter, "On the simulation of a class of time delay estimation algorithms," *IEEE Trans. Acoust. Speech Signal Processing*, vol. ASSP-29, pp. 534–540, 1981.
 - [45] A. Fertner and A. Sjolund, "Comparison of various time delay estimation methods by computer simulation," *IEEE Trans. Acoust. Speech Signal Processing*, vol. 34, pp. 1329–1331, 1986.
 - [46] L. A. Bohs, B. H. Friemel, B. A. McDermott, and G. E. Trahey, "A real-time system for quantifying and displaying two-dimensional velocities using ultrasound," *Ultrasound Med. Biol.*, vol. 19, pp. 751–761, 1993.
 - [47] R. B. Kuc, "Application of Kalman filtering techniques to diagnostic ultrasound," *Ultrason. Imag.*, vol. 1, pp. 105–120, 1979.
 - [48] K. W. Ferrara, V. R. Algazi, and J. Liu, "The effect of frequency dependent scattering and attenuation on the estimation of blood velocity using ultrasound," *IEEE Trans. Ultrason. Ferroelect. Freq. Cont.*, vol. 39, pp. 754–767, 1992.
 - [49] T. Loupas, R. B. Peterson, and R. W. Gill, "Experimental evaluation of velocity and power estimation for ultrasound blood flow imaging, by means of a two-dimensional autocorrelation approach," *IEEE Trans. Ultrason. Ferroelect. Freq. Cont.*, vol. 42, no. 4, pp. 688–698, Jul. 1995.



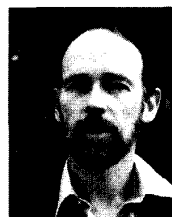
Thanasis Loupas received the B.E. degree in electrical engineering from the National Technical University of Athens, Greece in 1983. He was a post-graduate research student at the National Research Center "Democritos," Athens (1983–1984) and the Department of Medical Physics and Medical Engineering, University of Edinburgh, Scotland (1984–1988) from where he received the Ph.D. degree in 1988.

He stayed at the same Department until 1990 as a Research fellow, working on projects related to real-time image processing and Doppler ultrasound. After completing his compulsory national service in 1991, he joined the Institute of Information Science, ELKEPA, Athens as a project manager, responsible for initiating and coordinating EEC-funded projects in Informatics. Since 1992, he has been with the Ultrasonics Laboratory, CSIRO Division of Radiophysics, Sydney, Australia, where he is currently a Senior Research Scientist working on projects related to blood flow and medical image processing.



J. T. Powers received the B.A. in Physics in 1972 and the M.A. degree in bioengineering in 1974 from UCSD. He received the Ph.D. degree in electrical engineering from the University of Washington in 1980 working with the Center for Bioengineering.

From 1980 to 1981 he had a postdoctoral fellowship at the Kantonsspital Basel, Switzerland, to work in lasers and light scattering. He joined Advanced Technology Labs in Bothwell, WA in 1982. At Advanced Technology Labs he has worked in color flow signal processing, system architecture development, and beamformer design. He has also worked in contrast agent detection through collaborations with manufacturers and researchers. He is currently serving as Chief of the Senior Technology Staff. He holds six patents.



Robert W. Gill (S'67–M'74) was born in Sydney, Australia in 1945. He received the B.Sc. and B.E. degrees in electrical engineering from the University of Sydney in 1966 and 1968, respectively. He received the M.S. and Ph.D. degrees, also in electrical engineering, from Stanford University, CA in 1969 and 1975, respectively.

In 1975, he returned to Australia to take up a position with the Ultrasonics Institute (currently the Ultrasonics Laboratory of the CSIRO), where he continues to work. His major research interest has been Doppler ultrasound and its applications, including the measurement of volumetric flow. He has published more than 90 papers and presented invited papers at 20 international meetings.

Dr. Gill is a past President of the Australasian Society for Ultrasound in medicine, a Fellow of the Australasian College of Physical Scientists and Engineers in Medicine and an Honorary Fellow of the American Institute of Ultrasound in Medicine. He has helped to organize a number of conferences and workshops, and is the Editor of the Australasian Society for Ultrasound in Medicine newsletter.